Improved Mechanical Properties of β Metastable Ti alloys processed by Laser Powder Bed Fusion

A. Duchaussoy[1, 2], M. Marteleur[1], P.J. Jacques[1] and L. Choisez [1]

[1] *UCLouvain, Institute of Mechanics, Materials and Civil Engineering, IMAP, Place Sainte 2, B-1348 Louvain-la-Neuve, Belgium*
[2] *Now at Groupe de physique des matériaux, UMR CNRS 6634, Normandie Université, Avenue de l'université, 76800, Saint Etienne du Rouvray, France*

Abstract

This study proposes a thorough investigation of the mechanical properties of two β metastable titanium alloys (Ti-12Mo and Ti-8.5Cr-1.5Sn (wt %)) processed by laser powder bed fusion. Particular emphasis is put on the influence of chemical homogenization and defects formation as a function of the processing parameters. It is demonstrated that the Transformation / Twinning – induced plasticity (TRIP/TWIP) mechanisms already revealed as beneficial in the case of wrought alloys, still bring a larger work hardening level and a larger ductility in the case of laser powder bed fusion (L-PBF) processing. Improved mechanical properties in terms of yield and ultimate tensile strengths with similar uniform deformation compared to the wrought counterparts are thus achieved after L-PBF and a very short annealing.

Keywords: β metastable titanium alloys, LPBF, work hardening, strength, ductility

1. Introduction

The major advantage of metal additive manufacturing (AM), i.e. the ability to process fully operational complex parts in a unique operation, is nowadays largely hindered by the reduced number of compatible alloys and/or by the decreased levels of mechanical properties compared to conventionally processed equivalent parts. Among the thousands of available metallic alloys in use today, very few can be reliably printed without detrimental defects resulting from the specificities of the process, such as cyclic heating, melting/solidification, segregation, grain growth, … as summarized by Meier *et al*. [1]. Large efforts are currently done in developing the Laser Powder Bed Fusion (L-PBF) process of high-

performance engineering metallic materials initially inappropriate for AM like high strength Al 7xxx [2] and 2xxx [3] series, TiAl intermetallic compounds [4], Nitinol [5], etc.

Among recent high-performance metallic alloys, titanium alloys have seen the emergence of β metastable titanium alloys exhibiting simultaneously Transformation-induced martensitic transformation (TRIP) and mechanical twinning (TWIP) [6–10], leading to a significant increase in both strength and ductility, particularly in the case of wrought alloys. Furthermore, beside the improvement of the work hardening rate by the TRIP and TWIP effects [11,12], impressive fracture toughness and true fracture strain were also revealed in the case of the archetypal Ti – 12 wt % Mo alloy [13], related to an extraordinary resistance to damage nucleation [14]. Considering such alloys for additive manufacturing with its specific set of processing parameters could bring improved or at least undeteriorated properties.

Several β-type TRIP or TWIP alloys were recently processed by L-PBF, either in the case of pre-alloyed powders [15–17] or as *in-situ* alloying based on blended powders [18,19]. This technique promotes the manufacturing of parts with a blend of elemental powders instead of pre-alloyed powders, achieving alloying operation during the scanning of the laser beam. Combining different mixtures of powders and processing parameters opens up a whole new research field and it gets rid of the accessing problem to suitable feedstocks of atomized powders [20]. Collins *et al.* and Almeida *et al.* [21,22] showed that a hardness level close to the wrought case can be reached by this technique through laser cladding of Ti and Mo powders. However, depending on the printing and powders parameters, this method can lead to the formation of unmelted zones and/or chemical heterogeneities as with Ta [23], Nb [18,24–26] , V [21], Mo [19,21,22] or more elements [27] in the Ti matrix. This is mainly due to the large difference in particle sizes, melting points and densities of the elemental powders. This can be an obstacle in the achievement of a homogeneous microstructure and uniform distribution of the chemical elements in the SLM process. And the quantification of this inhomogeneity has never been carried out extensively.

The work of Vrancken *et al.* [19] showed that the presence of unmelted Mo particles in a β −stable Ti alloy does not seem to have visible influence on the mechanical properties (tensile and fatigue), as also pointed out by others studies [28,29]. Some authors showed that a deliberately heterogeneous material can be a means of achieving original mechanical properties [30] or tuned one for specific needs [23].

Unfortunately, the presence of unmelted powder more generally leads to a drop in mechanical properties. In particular, the design of β-metastable Ti alloys is highly compositionally-dependent, so that it is necessary to achieve sufficiently spread chemical homogenization in addition to optimizing the printing parameters to achieve fully dense microstructures. Duan *et al.* [31] reported that it is very challenging to print the Ti – 12 wt % Mo grade without remaining unmelted Mo particles. While Duan *et al.* [31] obtained a relatively homogeneous concentration of Mo by several remelting of the powders during the printing process, the reported large ductility and strain-hardening capacity of this alloy were lost together with the suppression of the TRIP and TWIP effects in the printed samples. A similar suppression of the TRIP and TWIP effects together with a strong decrease of ductility was reported by Mantri *et al.* [32] in the AM processed conditions of β-metastable Ti-10V-2Fe-3Al alloy, by Chen *et al.* [33] after printing high strength β − metastable Ti-6Mo-5.5Cr-1Co-0.1C alloy, and by Qui *et al.* [34] in Ti-10V-2Fe-3Al alloy. Mantri *et al.* [32] revealed through a combination of Transmission Electron Microscopy and Atom Probe Tomography the presence of fine α laths as well as a high density of ω nanoprecipitates in the as-printed β grains as well as zones of depleted alloying elements around these precipitates. They argued that the successive heat treatments undergone by the printed material during additive manufacturing favoured the growth of ω_{iso} and α precipitates, rejecting the β-stabilizing elements from the precipitates to the matrix and modifying locally the β-stability of the alloy. Some ductility (6% elongation) could be recovered by applying an annealing treatment on the printed alloy followed by water quenching to obtain a β-metastable microstructure, reactivating both TRIP and TWIP effects [32]. Although additive manufacturing of β −metastable Ti alloys has been studied to some extent, only relatively poor tensile ductility has been reported yet (max 6%), far from

the excellent ductility and strain-hardening capacity reported for wrought β −metastable Ti alloys [6–10].

The aim of this work is to study the potential of 3D printed β −metastable Ti alloys, in particular Ti – 12 wt % Mo and Ti - 8.5 wt % Cr - 1.5 wt % Sn alloys, in terms of mechanical properties. Pure elemental powders were mixed and processed by L-PBF using ranges of processing parameters in order to generate a wide range of microstructures potentially containing defects in several natures and proportions.

2. Experimental Procedure

Elemental powders of titanium (Grade 1, <45 µm in diameter), chromium (99% pure, <45 µm) and tin (99.7%, <45 µm) from TLS Technik and molybdenum (99.95%, 3-7 µm in diameter, agglomerated into 15-20 µm agglomerates) from Alfa Aesar were used as raw materials for the L-PBF of 2 different TRIP/TWIP alloys reported in the literature [9,11–13,35], i.e. Ti-12wt % Mo and Ti-8.5 wt % Cr-1.5wt % Sn, called Ti12Mo and TiCrSn in the following. The elemental powders were mixed in a turbula for several hours to ensure homogeneity of the blended powders. In addition, pre-alloyed Ti-6Al-4V powder was also provided by TLS Technik for the sake of comparison. The initial batches are presented in Figure 1, together with the powder size distributions (PSD). Mean diameters of 30, 25 and 23 µm were measured for Ti12Mo, TiCrSn and TA6V, respectively, while the D_{90} were 45, 36 and 33 µm.

TA6V and TiCrSn samples were fabricated using a DMP-X100 machine, while Ti12Mo samples, requiring more power (due to the high melting temperature of Mo), were fabricated using a DMP-X200 machine, both from 3D Systems, with pure Ti substrate. The layer thickness was 30 µm while the residual oxygen level of the Ar atmosphere was kept below 200 ppm during the whole fabrication cycles. Cubes 10*10*10 mm³ in size were printed for density measurements and microstructural characterization, while plates of 80*12*2 mm³ were printed for mechanical testing. All samples were fabricated with the hexagonal strategy available in the 3D Systems software. After separation from the substrate by

electrical discharge machining (EDM), 'dog-bone' shape tensile specimens were machined with a calibrated gauge length of 26 mm and a width of 6 mm. The thickness of the mechanically tested samples was the thickness of the as-built plates that were only ground with SiC paper to remove the excessive roughness since no contour optimization procedure has been carried out in this study. It is worth noting that the building direction (Z) is perpendicular to the tensile direction. The mechanical properties of the 3D printed specimens were measured using uniaxial tensile loading with a crosshead speed of 1 $mm.min^{-1}$. Details for the derivation of the engineering stress – engineering strain curves as well as true stress – true strain curves up to the true fracture point from the uniaxial tensile tests can be found in [14].

Wrought Ti-12Mo and Ti-8.5Cr-1.5Sn alloys were also processed to compare their mechanical properties to their 3D printed counterparts. Both alloys were cast by the self-consumable melting technique, with a nominal composition of Ti-12Mo-0.02Fe-0.01Cu-0.13O (wt.%) and Ti-8.51Cr-1.47Sn-0.04Fe-0.01Al-0.10O (wt.%). The cast alloys were then cold rolled with a 90% reduction level to a 1 mm-thick plate, recrystallized at 900°C for 15min and water quenched. The initial microstructure of both alloys is constituted of equiaxed β grains with an average initial grain size of 40 ± 9 µm for Ti-12Mo alloy and 86 ± 10 µm for Ti-8.5Cr-1.5Sn alloy. It should be noted that athermal ω_{ath} nanoprecipitates also form during water quenching, as demonstrated in [9, 11]. Wrought TA6V alloy was ordered from TIMET with a Widmanstatten microstructure. The initial microstructure of the wrought alloys can be found in Supplementary Materials (S1).

Density measurements of the 3D printed samples were performed both by the Archimedes method according to the ASTM-B311 procedure [36] using ethanol as wetting medium, and by light microscopy and automated image analysis using the ImageJ software. In the case of image analysis, porosities were first thresholded from the rest of the microstructure. The total porosity fraction as well as the pore size distribution were evaluated for each set of building parameters on a surface of 24 mm^2. The remaining unmelted or partially blended molybdenum particles (see below) were also included as

defects after the thresholding procedure, thus influencing the estimated proportion of 'porosities', which is then different from the densities estimated by the Archimedes' method. In the following, the term "defect" will therefore refer to either porosities or Mo particles unless the type of defect is explicitly specified.

Oxygen contents of the initial batches and of the as-fabricated parts were measured with a LECO ONH 836 system. SEM observations were carried out with FEG-SEM Ultra55 equipped with EDS and EBSD detectors.

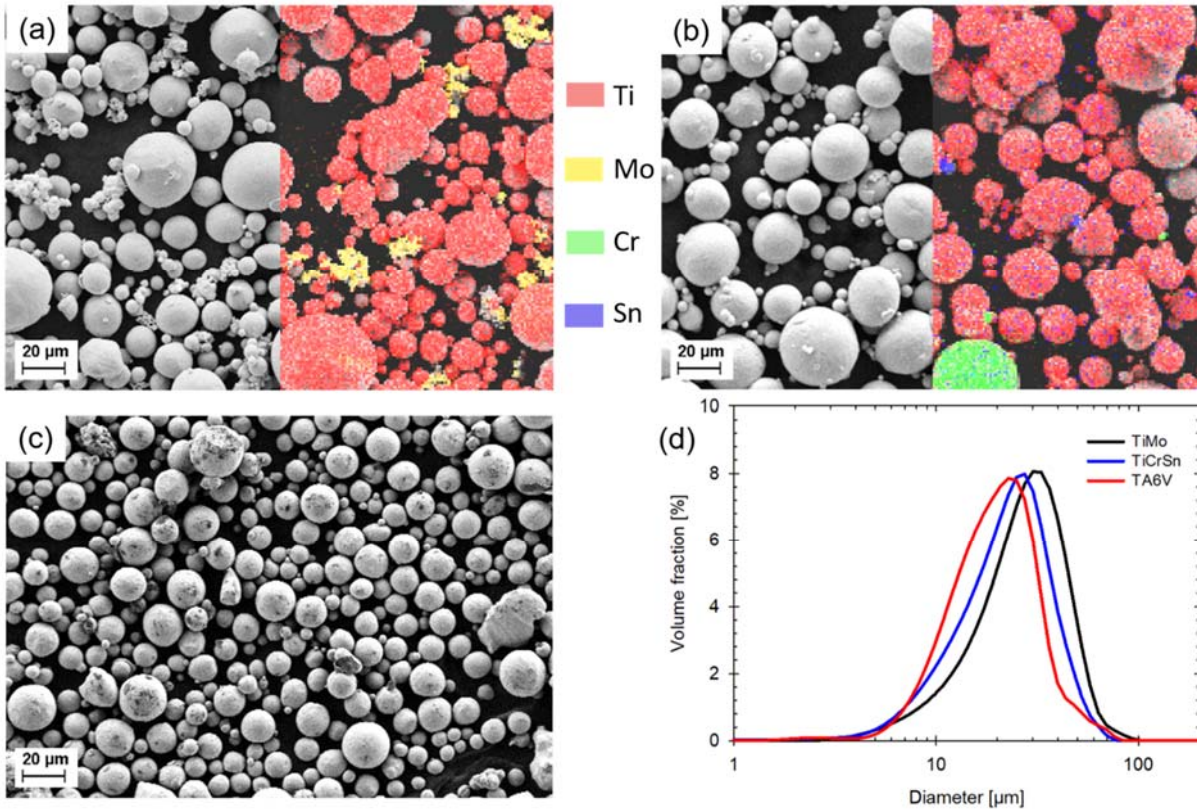

Figure 1: SEM and EDX micrographs of (a) Ti-Mo blend, (b) Ti-Cr-Sn blend and (c) Ti6Al4V powder. Pure Ti, Mo, Cr and Sn powder particles are shown in red, green, blue and yellow, respectively. The corresponding particle size distribution (PSD) are given in (d).

It is worth emphasizing that the optimization of the processing parameters in the case of blended powders is complexified with respect to the classical case of L-PBF processing of pre-alloyed powders.

Indeed, the classical optimization, which mainly consists in the minimization of the residual porosity, must be combined with other constraints which are the melting of pure elements, particularly presenting a high melting temperature like Mo (2610°C), and the in-situ homogenization of the resulting liquid. A preliminary study has been conducted in order to refine the process window in the case of Ti12Mo. A linear energy density parameter (defined as power/speed) ranging from 140 to 270 J m^{-1} was found to produce satisfactory results in terms of single-tracks shape and continuity. 22 different combinations of power level (P) and laser speed (S) were investigated, each time for two hatch spacings (hs), 50 and 70 µm. Power level P ranges from 80 to 275 W, laser speed S ranges from 300 to 1800 mm s^{-1}. Specific sets of parameters corresponding to various combinations of levels of porosity and chemical homogeneity will be presented in details in the following, even though the complete set of results will be considered in the case of mechanical properties. Finally, for TiCrSn and TA6V samples, the set of parameters optimized in a preliminary study will be considered.

3. Results and Discussion

3.1. Influence of the processing parameters on as-built microstructures

a) Density and defects

The density and characteristics of defects for the Ti12Mo grade were measured for a large range of processing parameters, resulting in a large range of defects quantities and sizes. Figure 2 presents typical optical micrographs of Ti12Mo when the relative density is larger than 99% (Fig. 2(a)) and when the relative density is smaller than 98% (Fig. 2(b)). Representative values are given in Table 1. In the case of TiCrSn and TA6V alloys, values are given for the samples with the highest levels of relative density. The complete dataset is given in Supplementary materials (S2).

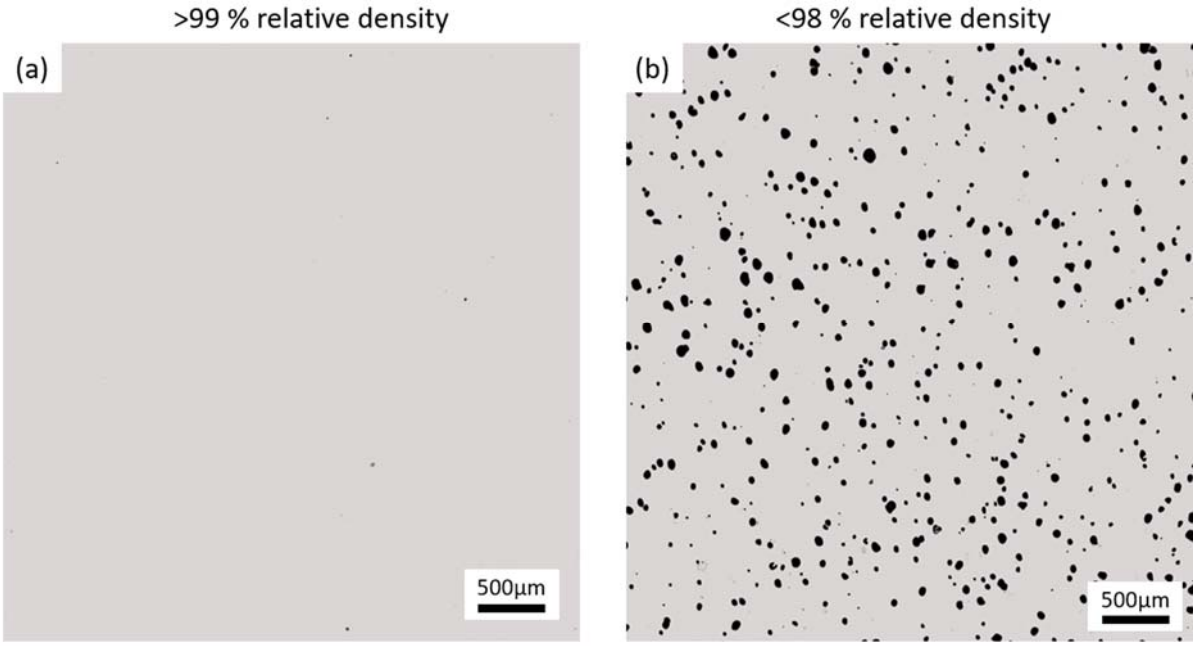

Figure 2: Light micrograph of Ti12Mo samples when the relative density is >99% (a) and <98% (b).

	P	***v***	***h***	***Archimedes relative density***	***Image based relative density***
	[W]	**[mm/s]**	**[µm]**	**[%]**	**[%]**
Ti12Mo	100	500	70	99.32	99.99
			50	99.09	99.06
		700	70	98.86	99.96
			50	99.39	98.94
	175	700	70	98.02	97.30
			50	97.24	96.39
		1200	70	99.34	99.98
			50	99.55	99.71
	275	1500	50	99.48	99.56
TiCrSn	100	800	70	99.02	99.08
TA6V	90	650	70	99.80	99.78

Table 1 : Archimedes and image based relative density obtained for focused sets of parameters.

As shown in Table 1, the relative density obtained for TA6V fits with the highest values reported in the literature (between 99 and 99.9%) [37–49]. In the case of Ti12Mo and TiCrSn samples, the relative density varies between 97.2% and 99.8%, which is in the range of the relative densities reported in previous work on Ti-Mo processed by L-PBF [50,51]. The mean pore radius is smaller than 10 µm for dense samples (>98% in relative density), and increases to the range of 10-20 µm for samples with a relative density <98%.

b) Oxygen content

The oxygen content of the processed samples was measured to assess a potential influence of the processing conditions on the level of dissolved oxygen and resulting mechanical properties. As shown in Figure 3, it is found that the oxygen picking is correlated to the volumetric injected energy defined as

$$E_{inj} = \frac{P*time}{volume}$$

where P is the power of the laser, '$time$' is the total building time of the sample used for oxygen measurement, and '$volume$' is the total volume of the sample. It is worth noting that this volumetric injected energy parameter E_{inj} is different from the energy density parameter *E* usually used in L-PBF (and defined as $E = \frac{P}{S*h*t}$ [J mm^{-3}], with S, h and t being the laser speed, the hatch spacing and the layer thickness, respectively). It is observed that the oxygen enrichment seems to follow a linear evolution with this parameter.

Figure 3 also shows that the oxygen level in Ti12Mo processed by L-PBF is of the same order of magnitude than in the case of wrought alloy. As the oxygen uptake is very low for all values of injected energies investigated in this work, it can be concluded that oxygen should not influence the triggering of expected plasticity mechanisms as shown in the case of wrought samples of Ti-10Mo-xO (wt.%) alloys by Min *et al*. [52].

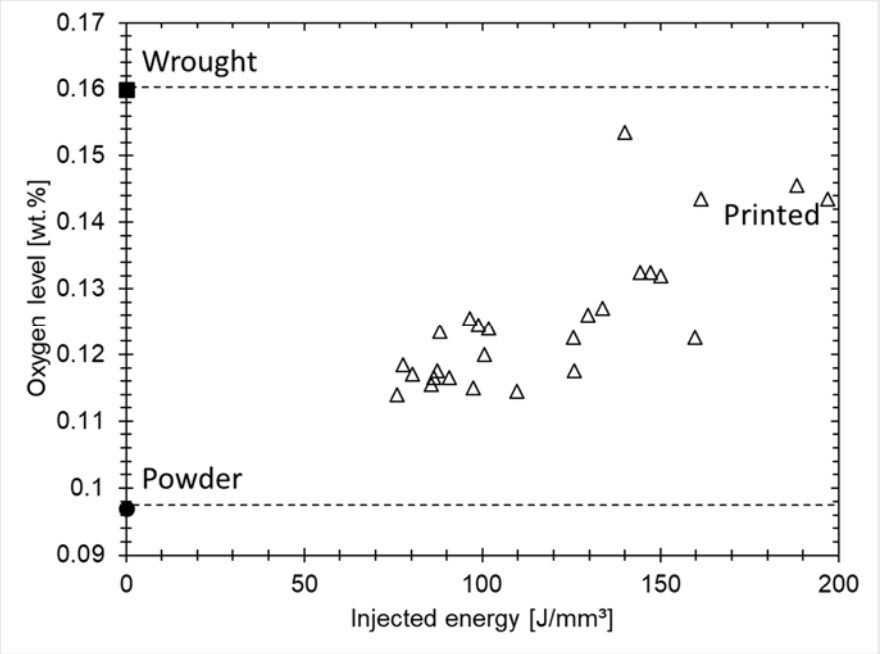

Figure 3: (a) Oxygen level as a function of the volumetric injected energy during printing of Ti12Mo. Oxygen levels of the powder and of the wrought state are also indicated.

c) Chemical homogeneity

As mentioned in the Introduction, in the case of blended elemental powders, the thermally-activated alloying has to be scrutinized, particularly in the case of hard-to-melt alloying elements such as Mo. Several processing conditions were thus considered, with the aim of characterizing the resulting homogenization after fast melting and cooling. This is still of more fundamental importance when considering the fact that the simultaneous activation of the TRIP and TWIP effects during deformation of β metastable Ti alloys occurs for a narrow range of compositions around a nominal one.

Figure 4 illustrates the as-built microstructure of Ti12Mo with building parameters P=275 W, S=1500 mm s^{-1} and hs=50 µm as characterized by EBSD (Figure 4(a) - band contrast map) or by EDS (Figure 4(b)). Figure 4(b) actually corresponds to a reconstructed chemical map for which pixels are discriminated based on compositional ranges. Indeed, depending on the Mo content, the phases

potentially present in rapidly cooled microstructures are HCP α' martensite (for 0<Mo<1 wt %), orthorhombic α'' martensite (for 1<Mo<8 wt %, with increasing amount of residual β phase) and finally a fully β microstructure for Mo>8 wt % [11,53–58]. It should be noted that for a compositional range from 8 wt % to 15 wt %, the β phase is metastable and ω_{ath} nanoprecipitates are also formed during the rapid cooling [11]. Chemical heterogeneities are clearly visible on this map, consisting in either remaining unmelted Mo clusters or Mo-depleted zones. Furthermore, the microstructure is composed of elongated grains along the building direction, as it is almost systematically observed in additively manufactured Ti alloys [59–61]. A magnification of a Mo-depleted zone is given in Figure 4(c). The band contrast map highlights needle-shaped precipitates with a thickness of hundreds of nanometers and a few micrometers in length. These needles have been indexed as martensite. It is worth noting that XRD measurements have also been performed on as-built samples, confirming the presence of β (BCC) and α'' (orthorhombic) phases of titanium, as well as sometimes peaks corresponding to pure Mo (BCC as well). However, the phase quantification method based on EDS was preferred to avoid texture-induced uncertainties in the Rietveld refinement of diffraction spectra or undiscriminated Ti-β and Mo in the case of EBSD measurements.

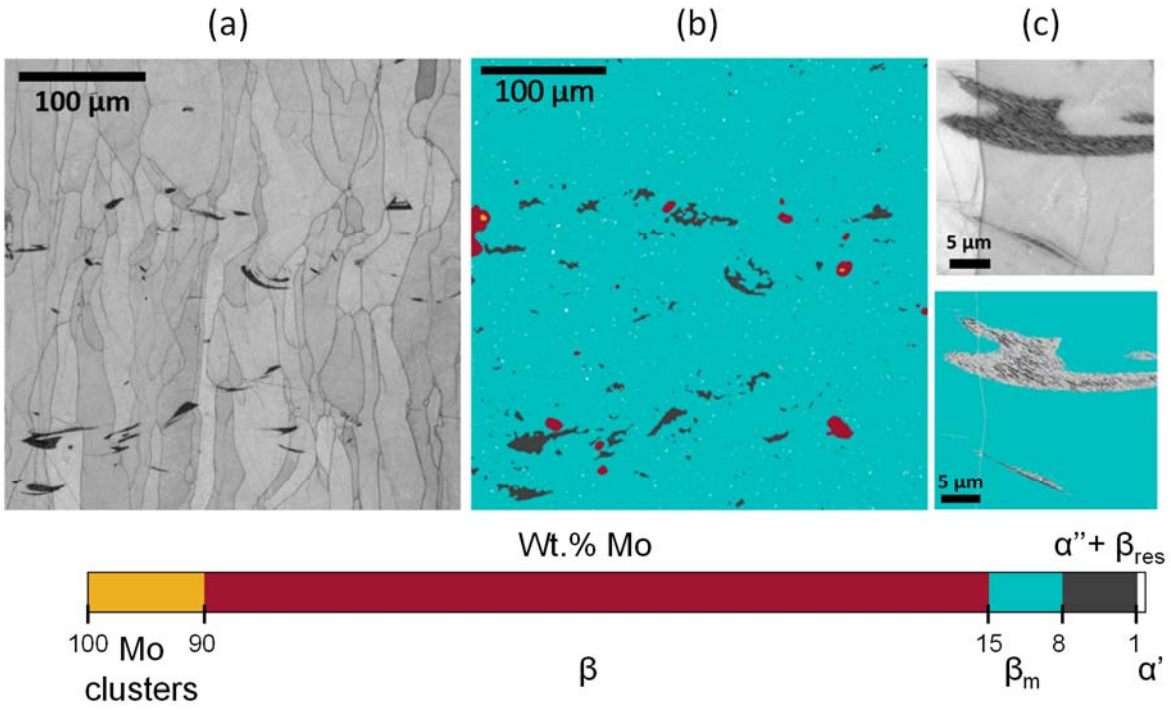

Figure 4: (a) Band contrast map of a Ti-12Mo sample processed by LPBF (P=275W, S=1500mm s^{-1}, hs=50 µm) and (b) reconstructed phase map from EDS mapping. (c) Magnified view of the dark features in (a) highlighting the martensitic needles of α'' phase (in dark grey) in the Mo-depleted zones. Light grey pixels correspond to unindexed pixels.

Figure 5 presents such phase maps based on EDS measurements for samples processed following the printing parameters given in Table 1. First, they show that decreasing the hatch spacing from 70 µm ((a), (c), (e) and (g)) to 50 µm ((b), (d), (f) and (h)) leads to less Mo-rich clusters in the Ti matrix. Secondly, increasing the speed is detrimental to the homogenization for a given level of power, contrarily to the influence of the increase of power for a given speed.

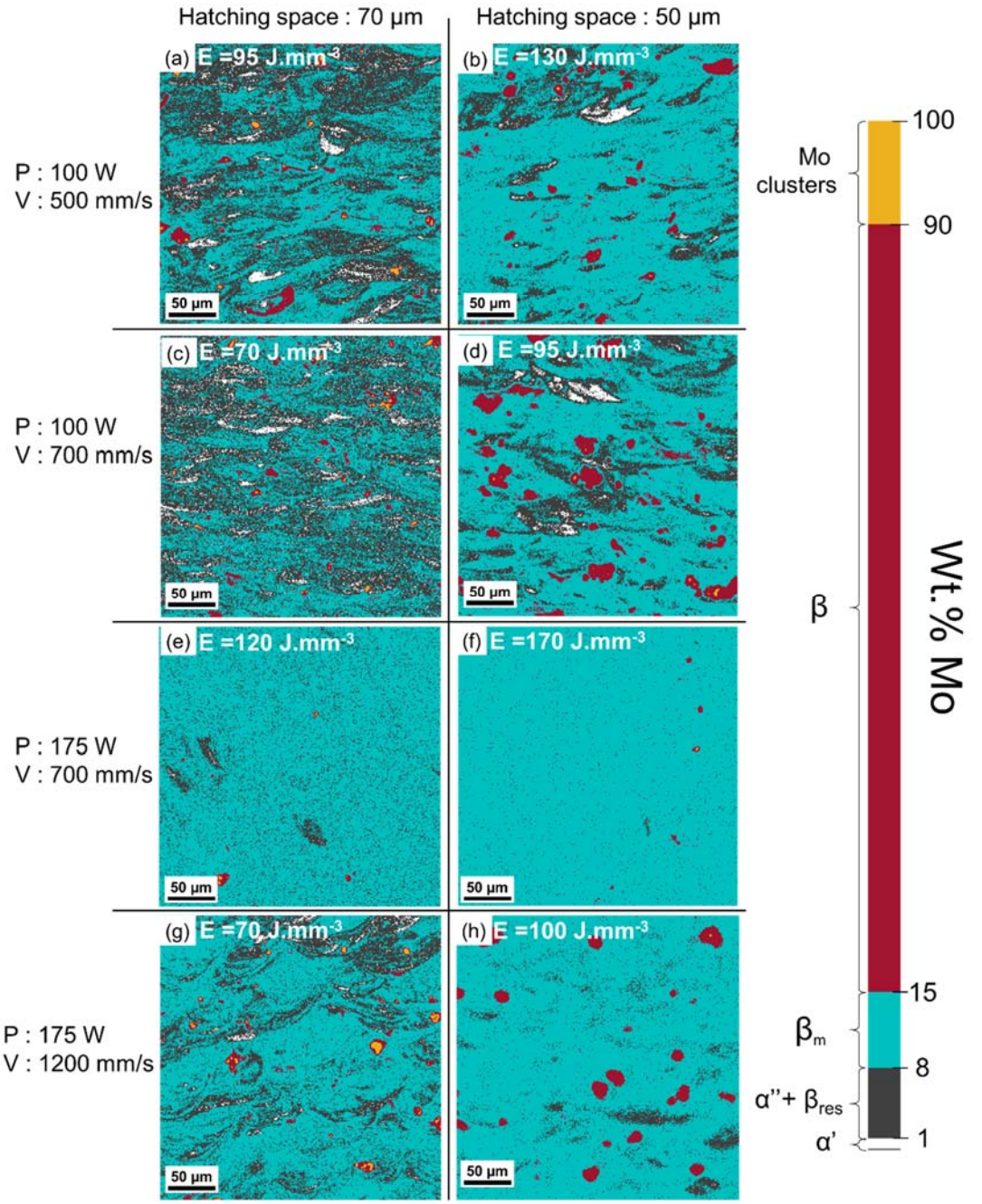

Figure 5: EDS-based phase maps of some Ti12Mo samples. Colors represent the Mo composition range of observable phases in the Ti-Mo system: white for α', grey for α'' (+β residual), cyan for metastable β, red for stabilized beta while yellow stands for Mo clusters. E as the energy density.

To assess the influence of such chemical heterogeneities, a single deviation to homogeneity criterion of processed microstructures has been defined. It consists in comparing the heterogeneous distribution of alloying elements with respect to the most homogeneous case taken as the reference (i.e. a wrought sample in the present case). Large EDS maps of 500*750 µm^2 have thus been measured

at the center of samples fabricated following each set of parameters. The size of these maps corresponds to a number of melt pools ranging from 75 to 125, depending on the orientation and hatch spacing (50 or 70 µm), which is considered as representative of the specific solidification process. The deviation to homogeneity criterion D is defined as follows:

$$D = \sum_{i=0}^{1} (x_i^{printed} - x_i^{wrought})^2$$

Where $x_i^{printed}$ and $x_i^{wrought}$ are the fractions of pixels of composition i (ranging from 0 to 1 and discretized by steps of 0.003) in a printed sample and in the wrought sample, respectively. A value of D close to 0 thus means a more homogenized microstructure. Figure 6 corresponds to the proportions of metastable β phase and of α'' + β_{res} as a function of this deviation factor. A monotonous increase of the proportion of β phase with the adequate composition (for the activation of the TRIP and TWIP effects – see below) is observed for decreasing D factor.

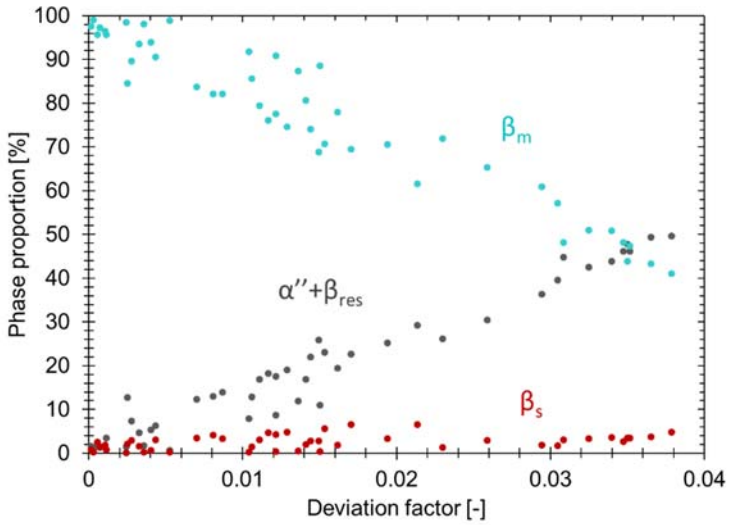

Figure 6: Evolution of the proportions of the main phases as a function of the deviation factor for all fabricated samples of Ti12Mo.

Figure 7 summarizes the deviation factor D calculated for numerous combinations of processing parameters. It can be seen that decreasing the hatch spacing has a first order effect on the homogenization (location of red and blue zones). On the other hand, homogenization is larger when

the lasing power is larger and when the lasing speed is slower. These observations can be rationalized through the size of the melt pools. Indeed, the melt pool size directly depends on the combination of lasing power and speed [62,63] thus fixing the number of re-melting cycles imposed to a given volume of material. Increasing the power, decreasing the speed and reducing the hatch spacing bring a larger number of re-melting cycles, resulting in a larger chemical homogenization. These observations are in good agreement with the results of Duan *et al.* [31].

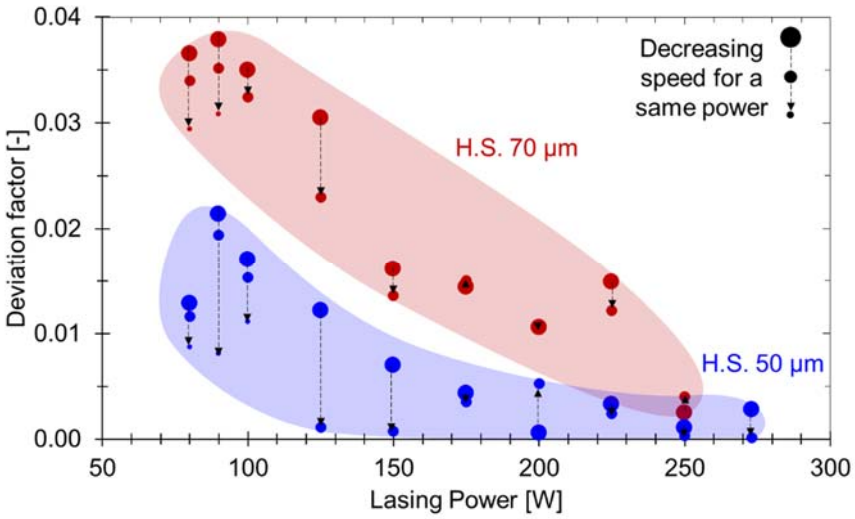

Figure 7: Deviation from homogeneity factor as a function of the lasing power and lasing speed (size of circles) for samples fabricated with 70 µm (red) and 50 µm (blue) hatch spacing for Ti12Mo alloy. Colored envelopes are guides for the eyes.

In the case of the TiCrSn alloy, a very low value of deviation to homogeneity factor (D=0.0058) has been reached, even with a hatch spacing of 70 µm. This observation can be explained by the fact that both Cr and Sn present lower melting temperatures with respect to titanium, resulting in an easier and more effective homogenization during the L-PBF processing.

Following the results of this analysis of the influence of the printing parameters on the as-built microstructures of Ti12Mo (but also on the mechanical properties which will be presented later in Figure 11), a sample was selected in order to be able to compare it to its wrought counterpart but also to the TiCrSn and TA6V alloys.

3.2. Mechanical properties of as-built and heat-treated microstructures.

a) Influence of heat treatment on microstructure, homogeneity level and mechanical properties of the three alloys

As in previous studies [17,32,64], mechanical properties of Ti alloys in as-built state show generally a brittle behaviour which can be easily overcome by post heat or thermomechanical treatment. Microstructures of Ti12Mo, TiCrSn and TA6V samples processed with optimized parameters are shown in Figure 8 in the as-built and heat-treated states. An annealing at 920°C for 2 hours under argon followed by air cooling (AC) was chosen for TA6V alloy to mimic the typical HIP treatment [65]. For Ti12Mo alloy, a short annealing at 900°C for 90 seconds in air was chosen at it was sufficient to recover its ductility, as discussed below, while hindering grain growth and oxygen intake. A longer heat treatment at 900°C for 15min was chosen for TiCrSn alloy to further increase its homogenization, which was not possible for Ti12Mo due to the low diffusivity of Mo. The process parameters in the case of Ti12Mo were P = 275 W and V = 1500 mm s^{-1}, bringing homogenization (D<0.001) and a low fraction of small porosities (Table 1). Typical columnar grains elongated along the building direction (Z) are observed (as already reported for Ti alloys [59,60]), together with remaining chemical heterogeneities associated to unmelted or partially melted clusters of Mo. Melt pool boundaries are clearly visible as depicted in the magnified inset of Figure 8(a). White lines correspond to the initiation of the planar solidification front that quickly turns into a fine dendritic solidification front. In the heat-treated Ti12Mo sample (Figure 8(b)), these white lines and fine dendrites are no longer visible. However, the former melt pool boundaries can still be guessed owing to the chemical contrast brought by the remaining local chemical heterogeneity. In the case of the TiCrSn as-built sample, some Cr particles were scarcely observed, but disappeared in the heat-treated conditions. Finally, microstructures of as-built and heat-treated TA6V samples are given in Figures 8(e) and (f), respectively. As-built microstructure consists of very fine acicular α' martensite as thoroughly studied previously [38,66–70]. Prior columnar β grains of hundreds of µm in height are present due to epitaxial growth during

solidification. Heat-treated microstructure (Figure 8(f)) on the other hand, exhibits a growth of α lamella, with β phase precipitation between them.

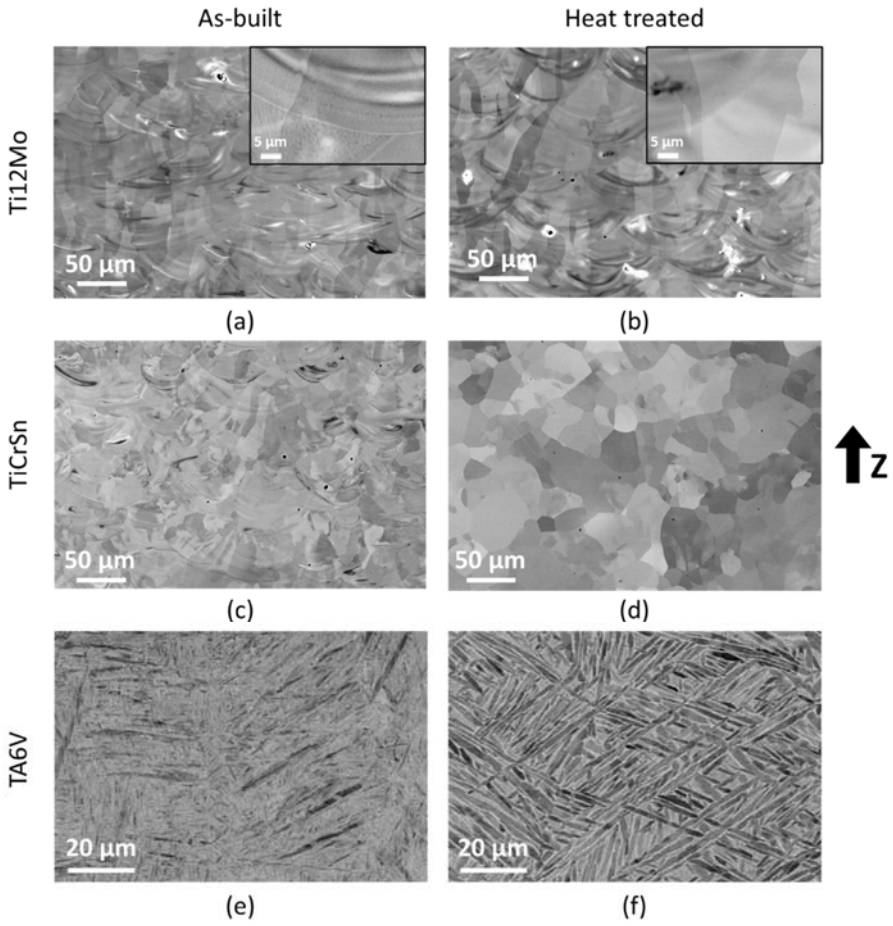

Figure 8: SEM micrographs of L-PBF processed alloys with building direction orientated vertically. (a) and (b), as-built (275 W, 1500 mm s^{-1}) and heat treated (90 s at 900°C + WQ) Ti12Mo, respectively. (c) and (d): TiCrSn as-built and heat-treated (15 min at 900°C + WQ), respectively. (e) and (f): TA6V as-built and heat treated (2h at 920°C + AC), respectively. Insets in (a) and (b) highlight melt pool boundaries.

A comparison of the EDS maps corresponding to the wrought, as-built and heat-treated states for Ti12Mo and TiCrSn alloys is given in Figure 9. In the case of TiCrSn, a treatment for 15min is sufficient to obtained a good chemical homogenization. This observation was consistently reproduced in several areas of the sample (supplementary material S3).

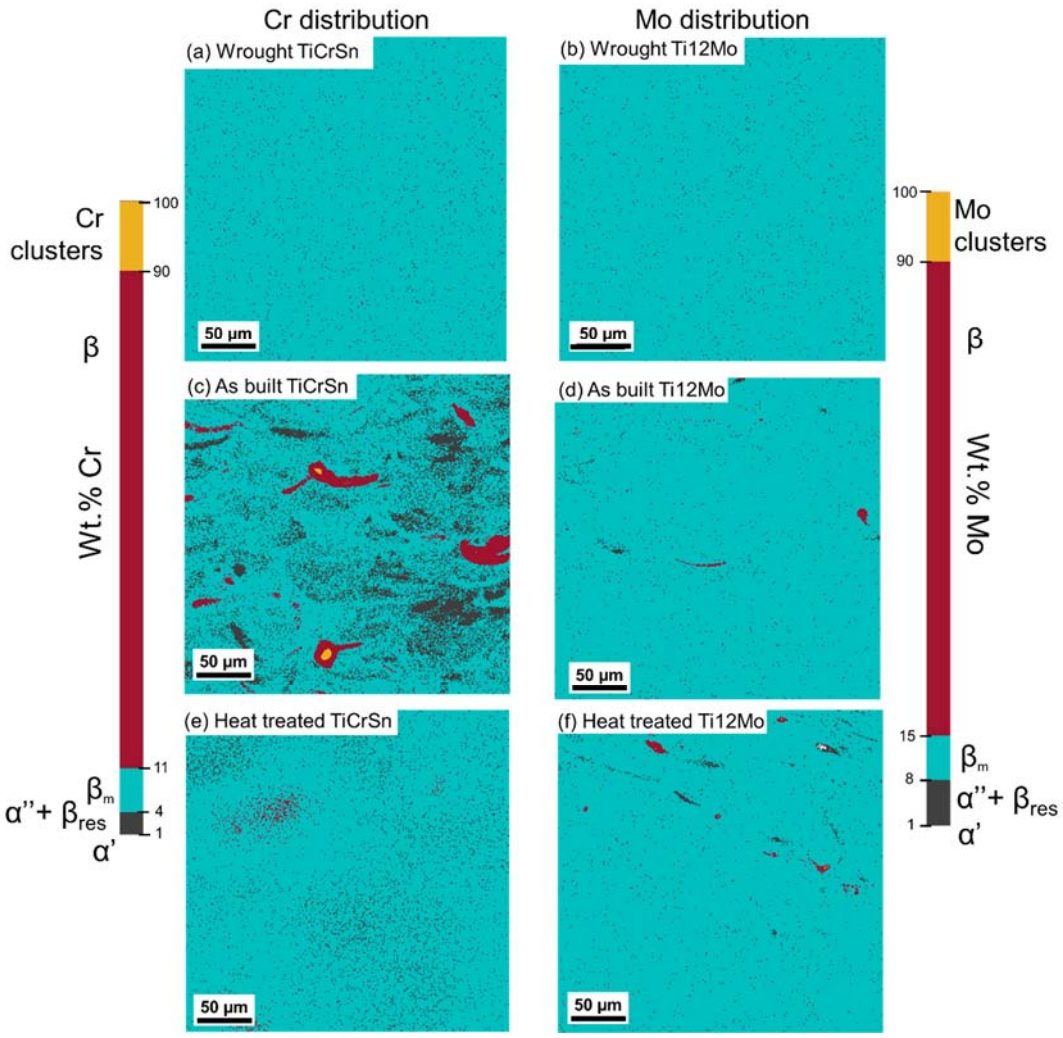

Figure 9: EDS-based phase maps of Cr in TiCrSn (a, c) and of Mo in Ti12Mo, 275 W, 1500 mm s^{1} (b, d) samples. In wrought (a, b) and printed + heat treated (c, d) states. Colors represent the composition range of observable phases in the Ti-Mo and Ti-Cr systems: white for α', grey for α'' (+β residual), cyan for metastable β, red for stabilized beta while yellow stands for Mo and Cr clusters.

Tensile curves of these as-built and heat-treated samples are given in Figure 10 for the 3 grades. For both TRIP/TWIP Ti12Mo and TiCrSn alloys, as-built samples show very high yield strength, larger than 1 GPa, but almost no uniform elongation. After annealing, both alloys recover a large ductility with a uniform elongation of 36% and 30% for Ti12Mo and TiCrSn, respectively. Heat treated Ti12Mo alloy exhibits a yield strength of 695 MPa with an ultimate tensile strength (UTS) of 820 MPa and TiCrSn grade exhibits yield and ultimate tensile strengths of 680 and 945 MPa, respectively. These levels of properties correspond to the typical ones obtained in the case of wrought TRIP/TWIP Ti alloys, even if the starting materials consisted in blended elemental powders. Interestingly, the short annealing

applied in the case of Ti12Mo is long enough to regenerate the mechanical properties from the as-built state. A similar recovery of ductility was observed in another β-metastable Ti alloy using a heat treatment over the β-transus temperature after 3D printing [32] and was associated with the growth of the initially present athermal ω_{ath} nanoprecipitates into the embrittling isothermal ω_{iso} nanoprecipitates. It was hypothesized that the coarsening of these ω_{ath} nanoprecipitates occurs during successive reheating associated with the consolidation of the successive layers, leading to a brittle behavior [32,33,71–73]. When globally reheated above the β-transus during the post-heat-treatment, these ω_{iso} precipitates are completely dissolved, regenerating the effective microstructure and ductility with the re-activation of both TRIP and TWIP effects in these β-metastable alloys. A similar growth of ω_{iso} nanoprecipitates during 3D printing is expected in the case of β −metastable Ti12Mo and TiCrSn alloys as supported by the full recovery of their ductility after a heat treatment over the β-transus temperature, followed by water quenching. In the case of TiCrSn, a longer heat treatment of 15 minutes was applied not only to regenerate the β phase, but also to erase the Cr heterogeneities. Finally, the tensile curves of TA6V in as-built and stress-relieved conditions are also given in Figure 10 for the sake of comparison. This heat treatment brings some softening with a slight increase of the deformation.

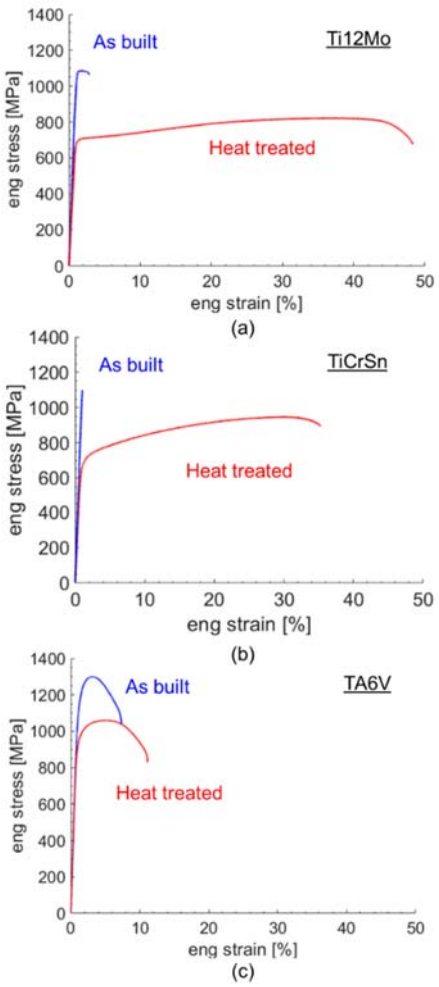

Figure 10: Engineering tensile stress-strain curves of Ti12Mo (a), TiCrSn (b) and TA6V (c) alloys in L-PBF as-built conditions (blue curves) and after heat treatment (red curves).

Figure 11 presents SEM and EBSD analyses of deformed microstructures of heat-treated Ti-12Mo and Ti-8.5Cr-1.5Sn alloys. A dense network of deformation features is observed, resulting from the activation of the TRIP and TWIP effects, as expected from previous studies [9,11].

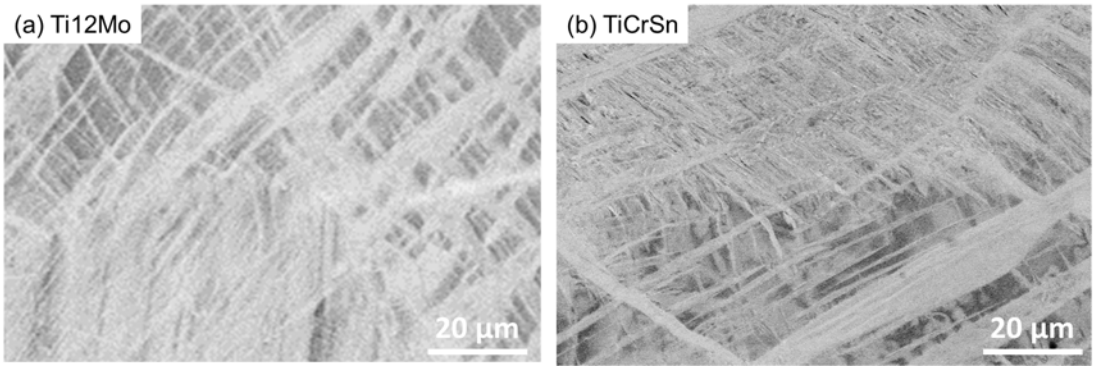

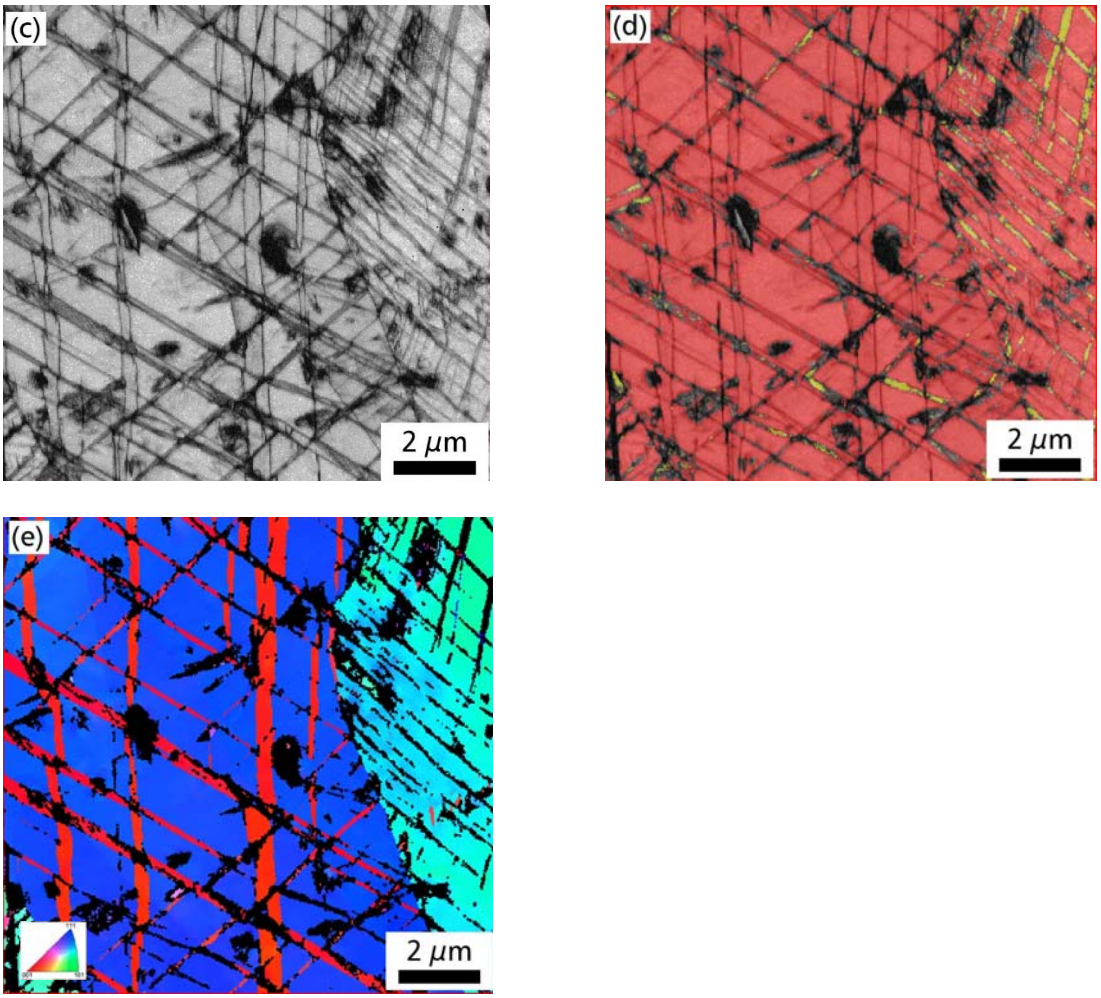

Figure 11: SEM and EBSD micrographs of strained Ti12Mo (a, c, d, e) and TiCrSn (b) samples processed by L-PBF, illustrating the activation of the TRIP and TWIP effects. Samples were deformed to ε=0.05. Map (c) corresponds to the band contrast; map (d) shows that martensite (in yellow) is present together with the β matrix; map (e) corresponds to the inverse pole map of the β phase, illustrating the occurrence of twinning.

b) Influence of the homogenization level and defects on the mechanical properties

Figure 12 illustrates the engineering stress – strain curves of heat-treated Ti12Mo samples after different processing conditions, thus presenting different amounts of defects (chemical heterogeneities and porosities) scrutinized above. The as-built curves are not given since it was shown in the previous section that a short annealing is mandatory to restore the TRIP/TWIP properties. A wide range of mechanical properties results from the investigated processing parameters. Particularly,

the ductility ranges from an elongation at fracture of less than 1% (fracture before the onset of plasticity) up to 50%. Interestingly, a lower spread of the mechanical properties can be observed for samples built with a hatch spacing of 50 µm, which present a larger chemical homogeneity as shown in Figure 7. The complete set of tensile curves is given in Supplementary materials (S4).

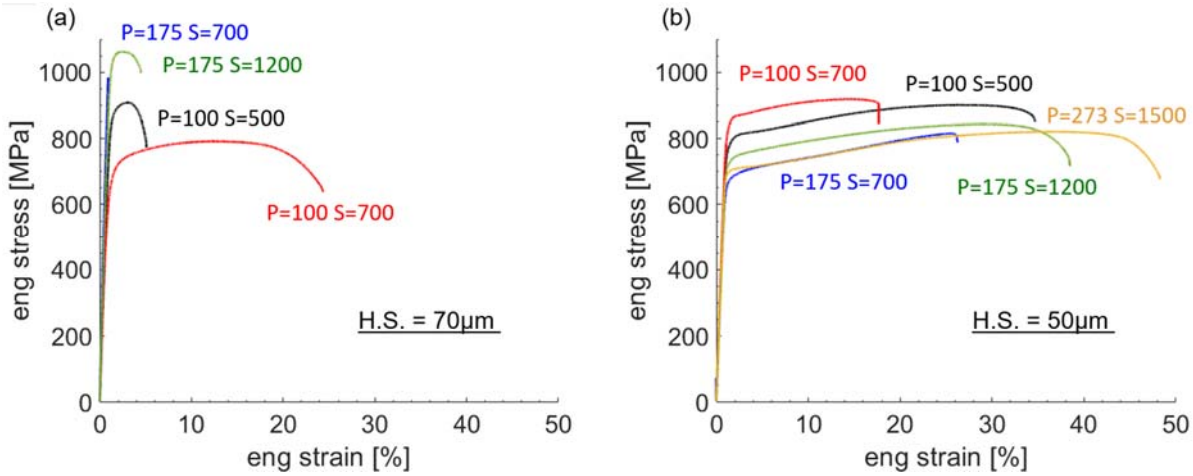

Figure 12: Effect of processing parameters (power (P) and speed (S)) on the mechanical properties of Ti12Mo processed by L-PBF and heat treated. Curves in (a) and (b) correspond to 70 µm and 50 µm of hatch spacing, respectively.

Figures 13(a) to (d) highlight 4 representative features that can be observed on the fracture surfaces of printed Ti12Mo: (i) small flat dimples (Figure 13(a)), (ii) very large dimples surrounded by smooth shear surfaces (Figure 13(b)), (iii) small broken particles in a ductile, teared matrix (Figure 13(c)), and/or (iv) very small dimples (around 100 nm in diameter, Figure 13(d)). The first fracture feature (Fig. 13(a)) is similar to what has been observed on the fracture surface of wrought Ti12Mo [14], and constitutes the main fracture feature of the most ductile 3D printed samples. It was shown that these flat dimples are associated to a large resistance to damage nucleation, forcing the formation of thin localized shear bands after strong localized necking at high true strain levels [14]. That feature is therefore associated with high ductility in terms of true fracture strain. In the most ductile 3D printed sample, these flat dimples are accompanied by either large cavities, as illustrated in Fig. 13(b), or by the third fracture feature (illustrated in Fig. 13(c)). The former originates from the initially present large porosities, while the latter originates from void nucleation events by fracture of small particles, identified as Mo-rich

particles by EDS, and/or decohesion between these particles and the matrix. As a large ductility is kept with the presence of initial large cavities and/or unmelted Mo particles, their presence does not constitute strongly embrittling features for these alloys. The relative unsensitivity of the ductility of the alloys on the presence of cavities and unmelted Mo particles is currently under investigation.

On the other hand, the fourth fracture feature (Fig. 13(d)) is observed in the case of the less ductile specimens, also corresponding to the less homogeneous specimens. Such small dimples are typically observed on the fracture surface of Ti alloys containing fine α/α' laths in a β matrix [14]. Unlike the initial Mo particles and initial voids, the presence of these α/α' laths in the initial microstructure, resulting from a low homogeneity level, seems to be detrimental to the ductility of the 3D printed Ti-12Mo alloys.

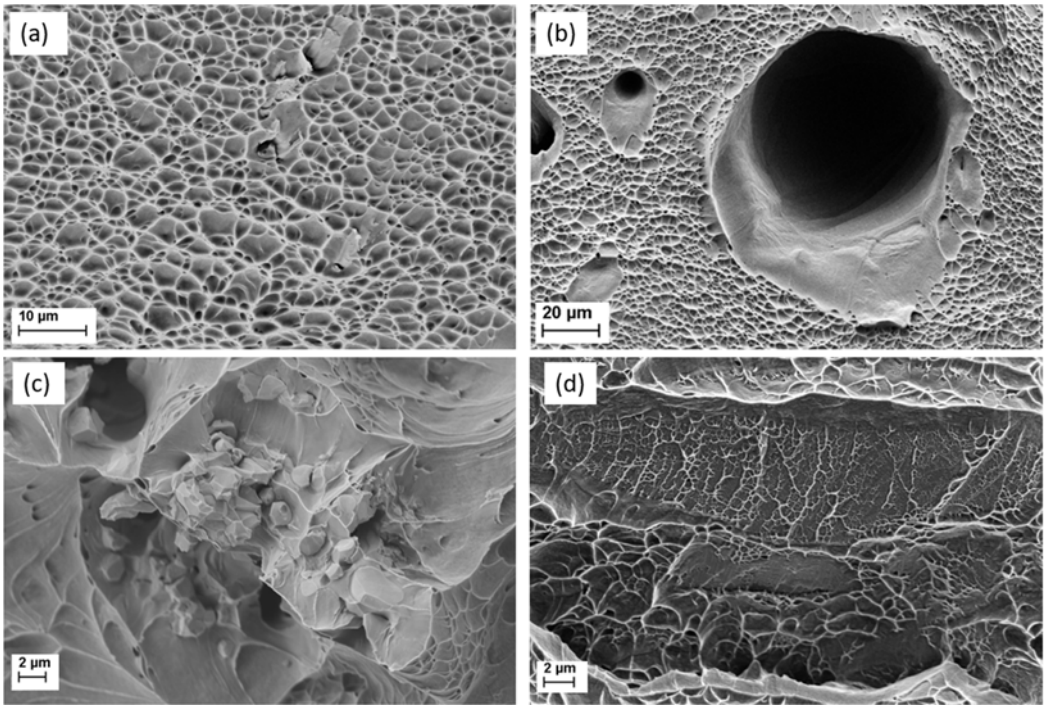

Figure 13: Representative SEM micrographs of the fracture surface. Processing conditions of sample corresponding to (a) 270 W-1800 mm s^{-1}-50 µm; (b) 175 W-700 mm s^{-1}50 µm; (c) 100 W-700 mms^{-1} 50 µm and (d) 175W-1200 mm s^{-1}-70 µm.

This study shows that a wide range of homogeneity levels, density and phase fractions (β, β-metastable, α/α') can be achieved depending on the chosen laser parameters, resulting in a wide range of associated mechanical properties. Moreover, these alloys exhibit a low sensitivity to the presence of defects inherently present with LPBF processing, in particular the presence of unmelted Mo particles, as it was already showed by previous work [19,28,29], but also the presence of initial porosities which is remarkable, especially for porosities of such a large size (10-20µm) that is uncommonly reported in the literature. This observation is in phase with the unique properties of damage and fracture of such alloys reported above and also in the case of wrought state [11,13,14].

c) Comparison with wrought TRIP/TWIP alloys

The excellent combination of both mechanical resistance and ductility of 3D printed Ti alloys is further highlighted in Figures 14 and 15, in comparison with their wrought counterparts and additively-processed TA6V alloys. Quite uniquely, the samples processed by L-PBF present improved mechanical properties, i.e. yield strength, UTS, uniform elongation and work hardening. Indeed, alloys processed by L-PBF classically present a higher yield strength but lower levels of ductility compared to their wrought counterparts as illustrated by TA6V on Figures 14 and 15 [37–47,69,74–78]. On the one hand, the increase of the yield strength in additively-processed samples is inferred to the finer microstructures resulting from rapid solidification [79]. On the other hand, ductility is generally decreased due to higher content of microstructural defects, which promote the damage mechanisms and crack propagation. Some exceptions must be highlighted, where the strength-ductility trade-off of classical additive manufactured alloys such as TA6V [80] and 316L [81] alloys could be increased by favouring nano-twinning through a controlled microstructure (texture, grain size). Agrawal *et al* [82] also showed a significant increase of yield strength, ultimate strength and uniform elongation in a 3D printed Fe-Mn-Co-Cr-Si high entropy alloy compared to its as cast counterpart, due to an enhanced TRIP and TWIP plasticity. In this study, at the end of the optimization of the processing parameters,

the two investigated grades of TRIP/TWIP Ti alloys also show quasi-static mechanical properties that are equal or better with respect to their wrought counterparts (Figure 14), particularly the work hardening rate. The origin of such improved mechanical properties could be explained by the synergy of several microstructural parameters such as finer microstructure and texture effects, which are controlled by the chosen set of printing parameters. But also, by the activation of the TRIP and TWIP mechanisms which indirectly depend on the chosen printing parameters via the chemical homogeneity of Mo in the Ti matrix. This will be investigated in a near future.

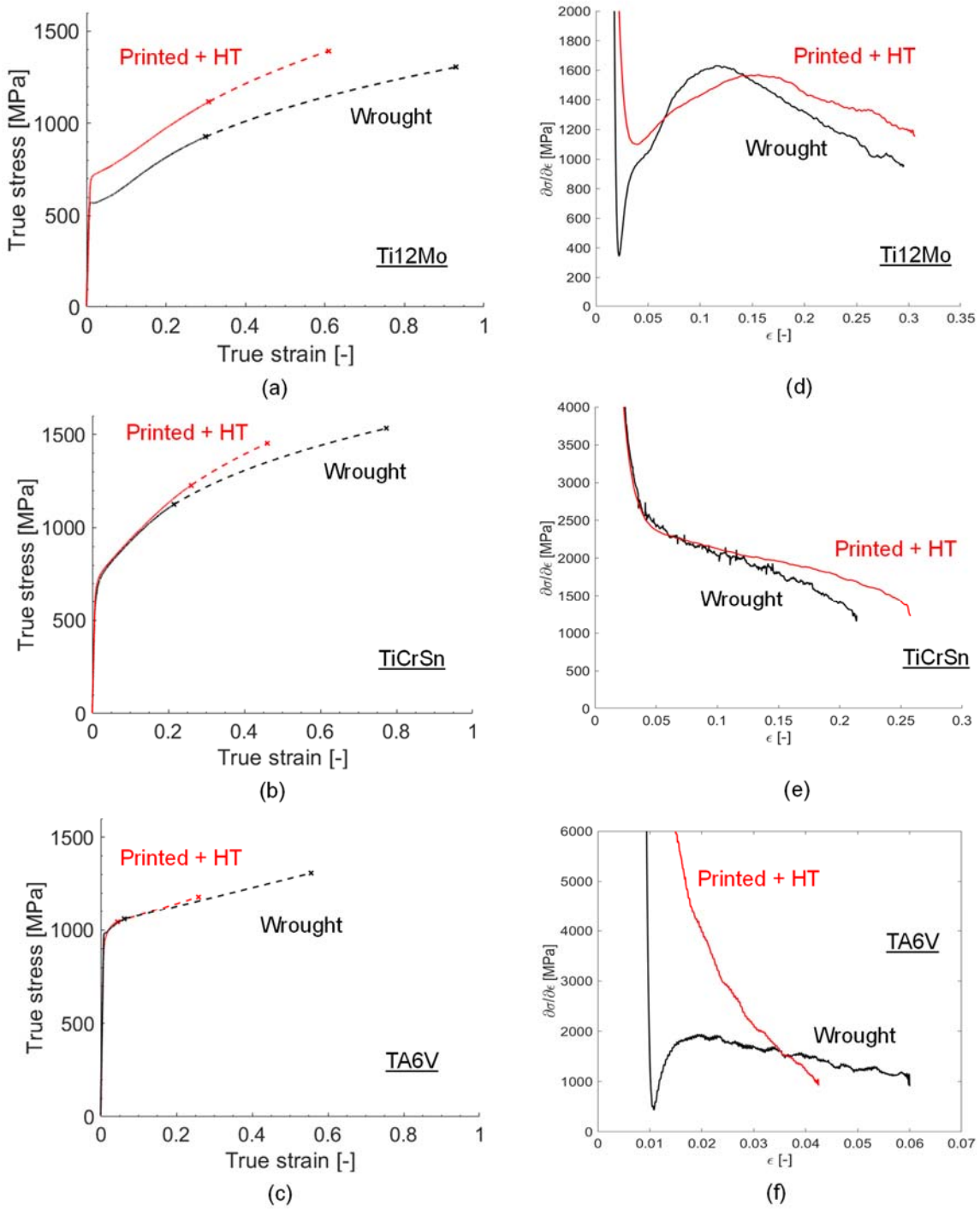

Figure 14: Tensile and work hardening curves of TiMo (a, d), TiCrSn (b, e) and TA6V (c, f) alloys after printing by L-PBF and heat treatment (red) compared to their wrought counterparts (black). dotted line parts of the tensile curves correspond to the extrapolation between the true uniform strain and true fracture strain.

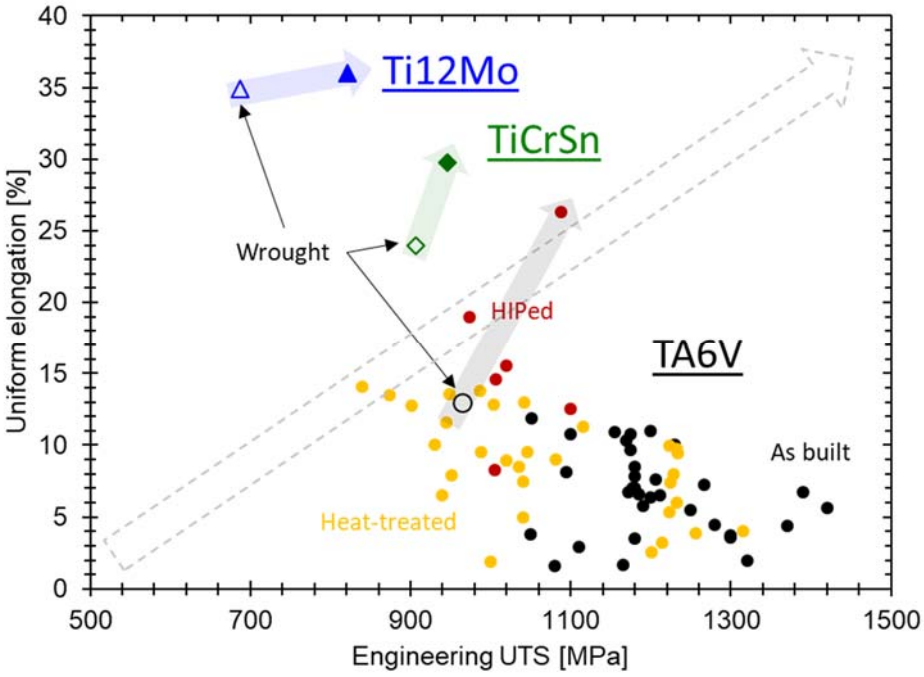

Figure 15: Combinations of uniform elongation and UTS for Ti12Mo (blue) TiCrSn (green) and TA6V (black, yellow, red) [37–47,69,74–76] for the wrought state (empty markers) and after printing (full markers). For TA6V, a distinction is made between the as-built state (black), annealed state (by pre-lasing, by hot building plate, or post printing treatment) (yellow) and HIP treatments (red).

4. Conclusion

This work investigated homogenization level and defects formation in β metastable titanium alloys processed by L-PBF and their influence on the resulting mechanical properties, in the case of blended powders as feedstocks. Two different alloys (Ti-12Mo and Ti-8.5Cr-1.5Sn (wt %)) were processed by *in-situ* alloying by L-PBF. The process is complexified by the presence of high melting point elements like Mo resulting in incomplete homogenization and/or porosity formation. As-built conditions exhibited brittle-like behavior, most probably due to the presence of ω_{iso} phase that coarsened during the successive processed-induced heat cycles. However, a very short annealing above the β transus was enough to recover excellent mechanical properties associated to the activation of the TRIP and TWIP effects.

Using blended powders as feedstocks allowed a thorough analysis of the influence of defects and homogeneity on the mechanical properties. A decrease in the relative amount of β −metastability together with the presence of α/α' laths due to insufficient homogenization was found detrimental for the ductility. However, more homogeneous samples exhibit a large strength - ductility balance. Furthermore, equal or improved work hardening and strength-ductility tradeoff was obtained in the L-PBF alloys compared to their conventionally processed, wrought, counterparts.

Further investigation is needed to understand the quantitative influence of the different defects (fine α/α' laths; unmelted Mo particles; porosities) and their synergy on the ductility and associated fracture mechanisms. Complementary investigations of the local mechanical behavior close to defects will be carried out.

Acknowledgments

The Fonds National de Recherche Scientifique FNRS is gratefully acknowledged for the grant n°T.0127.19 and the postdoctoral grant of L. Choisez.

Data availability

The datasets generated during and/or analyzed during the current study are available from the corresponding author on reasonable request.

References

[1] C. Meier, R.W. Penny, Y. Zou, J.S. Gibbs, A.J. Hart, THERMOPHYSICAL PHENOMENA IN METAL ADDITIVE MANUFACTURING BY SELECTIVE LASER MELTING: FUNDAMENTALS, MODELING, SIMULATION, AND EXPERIMENTATION, Annu. Rev. Heat Transf. 20 (2017) 241-316. https://doi.org/10.1615/AnnualRevHeatTransfer.2018019042

[2] N. Kaufmann, M. Imran, T.M. Wischeropp, C. Emmelmann, S. Siddique, F. Walther, Influence of Process Parameters on the Quality of Aluminium Alloy EN AW 7075 Using Selective Laser Melting (SLM), Phys. Procedia. 83 (2016) 918–926. https://doi.org/10.1016/j.phpro.2016.08.096.

[3] H. Zhang, H. Zhu, T. Qi, Z. Hu, X. Zeng, Selective laser melting of high strength Al–Cu–Mg alloys: Processing, microstructure and mechanical properties, Mater. Sci. Eng. A. 656 (2016) 47–54. https://doi.org/10.1016/j.msea.2015.12.101.
[4] M. Doubenskaia, A. Domashenkov, I. Smurov, P. Petrovskiy, Study of Selective Laser Melting of intermetallic TiAl powder using integral analysis, Int. J. Mach. Tools Manuf. 129 (2018) 1–14. https://doi.org/10.1016/j.ijmachtools.2018.02.003.
[5] M. Elahinia, N. Shayesteh Moghaddam, M. Taheri Andani, A. Amerinatanzi, B.A. Bimber, R.F. Hamilton, Fabrication of NiTi through additive manufacturing: A review, Prog. Mater. Sci. 83 (2016) 630–663. https://doi.org/10.1016/j.pmatsci.2016.08.001.
[6] L. Lilensten, Y. Danard, C. Brozek, S. Mantri, P. Castany, T. Gloriant, P. Vermaut, F. Sun, R. Banerjee, F. Prima, On the heterogeneous nature of deformation in a strain-transformable beta metastable Ti-V-Cr-Al alloy, Acta Mater. 162 (2019) 268–276. https://doi.org/10.1016/j.actamat.2018.10.003.
[7] S. Sadeghpour, S.M. Abbasi, M. Morakabati, A. Kisko, L.P. Karjalainen, D.A. Porter, A new multi-element beta titanium alloy with a high yield strength exhibiting transformation and twinning induced plasticity effects, Scr. Mater. 145 (2018) 104–108. https://doi.org/10.1016/j.scriptamat.2017.10.017.
[8] L. Ren, W. Xiao, C. Ma, R. Zheng, L. Zhou, Development of a high strength and high ductility near β-Ti alloy with twinning induced plasticity effect, Scr. Mater. 156 (2018) 47–50. https://doi.org/10.1016/j.scriptamat.2018.07.012.
[9] C. Brozek, F. Sun, P. Vermaut, Y. Millet, A. Lenain, D. Embury, P.J. Jacques, F. Prima, A β-titanium alloy with extra high strain-hardening rate: Design and mechanical properties, Scr. Mater. 114 (2016) 60–64. https://doi.org/10.1016/j.scriptamat.2015.11.020.
[10] J. Zhang, J. Li, G. Chen, L. Liu, Z. Chen, Q. Meng, B. Shen, F. Sun, F. Prima, Fabrication and characterization of a novel β metastable Ti-Mo-Zr alloy with large ductility and improved yield strength, Mater. Charact. 139 (2018) 421–427. https://doi.org/10.1016/j.matchar.2018.03.031.
[11] M. Marteleur, F. Sun, T. Gloriant, P. Vermaut, P.J. Jacques, F. Prima, On the design of new β-metastable titanium alloys with improved work hardening rate thanks to simultaneous TRIP and TWIP effects, Scr. Mater. 66 (2012) 749–752. https://doi.org/10.1016/j.scriptamat.2012.01.049.
[12] F. Sun, J.Y. Zhang, M. Marteleur, T. Gloriant, P. Vermaut, D. Laillé, P. Castany, C. Curfs, P.J. Jacques, F. Prima, Investigation of early stage deformation mechanisms in a metastable β titanium alloy showing combined twinning-induced plasticity and transformation-induced plasticity effects, Acta Mater. 61 (2013) 6406–6417. https://doi.org/10.1016/j.actamat.2013.07.019.
[13] L. Choisez, L. Ding, M. Marteleur, H. Idrissi, T. Pardoen, P.J. Jacques, High temperature rise dominated cracking mechanisms in ultra-ductile and tough titanium alloy, Nat. Commun. 11 (2020) 2110. https://doi.org/10.1038/s41467-020-15772-1.
[14] L. Choisez, A. Elmahdy, P. Verleysen, P.J. Jacques, Fracture mechanisms in flat and cylindrical tensile specimens of TRIP-TWIP β-metastable Ti-12Mo alloy, Acta Mater. 220 (2021) 117294. https://doi.org/10.1016/j.actamat.2021.117294.
[15] L.C. Zhang, D. Klemm, J. Eckert, Y.L. Hao, T.B. Sercombe, Manufacture by selective laser melting and mechanical behavior of a biomedical Ti–24Nb–4Zr–8Sn alloy, Scr. Mater. 65 (2011) 21–24. https://doi.org/10.1016/j.scriptamat.2011.03.024.
[16] T. Ishimoto, K. Hagihara, K. Hisamoto, S.-H. Sun, T. Nakano, Crystallographic texture control of beta-type Ti–15Mo–5Zr–3Al alloy by selective laser melting for the development of novel implants with a biocompatible low Young's modulus, Scr. Mater. 132 (2017) 34–38. https://doi.org/10.1016/j.scriptamat.2016.12.038.
[17] M. Duport, P. Lhuisser, J.-J. Blandin, R. Dendievel, M. Veron, F. Prima, G. Martin, Processing, microstructures and mechanical response of a β-metastable Ti-14Mo alloy fabricated by Electron Beam Powder Bed Fusion, Addit. Manuf. 61 (2023) 103340. https://doi.org/10.1016/j.addma.2022.103340.

[18] M. Fischer, D. Joguet, G. Robin, L. Peltier, P. Laheurte, In situ elaboration of a binary Ti–26Nb alloy by selective laser melting of elemental titanium and niobium mixed powders, Mater. Sci. Eng. C. 62 (2016) 852–859. https://doi.org/10.1016/j.msec.2016.02.033.
[19] B. Vrancken, L. Thijs, J.-P. Kruth, J. Van Humbeeck, Microstructure and mechanical properties of a novel β titanium metallic composite by selective laser melting, Acta Mater. 68 (2014) 150–158. https://doi.org/10.1016/j.actamat.2014.01.018.
[20] T. DebRoy, H.L. Wei, J.S. Zuback, T. Mukherjee, J.W. Elmer, J.O. Milewski, A.M. Beese, A. Wilson-Heid, A. De, W. Zhang, Additive manufacturing of metallic components – Process, structure and properties, Prog. Mater. Sci. 92 (2018) 112–224. https://doi.org/10.1016/j.pmatsci.2017.10.001.
[21] P.C. Collins, R. Banerjee, S. Banerjee, H.L. Fraser, Laser deposition of compositionally graded titanium–vanadium and titanium–molybdenum alloys, Mater. Sci. Eng. A. 352 (2003) 118–128. https://doi.org/10.1016/S0921-5093(02)00909-7.
[22] A. Almeida, D. Gupta, C. Loable, R. Vilar, Laser-assisted synthesis of Ti–Mo alloys for biomedical applications, Mater. Sci. Eng. C. 32 (2012) 1190–1195. https://doi.org/10.1016/j.msec.2012.03.007.
[23] S.L. Sing, W.Y. Yeong, F.E. Wiria, Selective laser melting of titanium alloy with 50 wt% tantalum: Microstructure and mechanical properties, J. Alloys Compd. 660 (2016) 461–470. https://doi.org/10.1016/j.jallcom.2015.11.141.
[24] J. Wang, Y. Liu, C.D. Rabadia, S.-X. Liang, T.B. Sercombe, L.-C. Zhang, Microstructural homogeneity and mechanical behavior of a selective laser melted Ti-35Nb alloy produced from an elemental powder mixture, J. Mater. Sci. Technol. 61 (2021) 221–233. https://doi.org/10.1016/j.jmst.2020.05.052.
[25] J.C. Wang, Y.J. Liu, P. Qin, S.X. Liang, T.B. Sercombe, L.C. Zhang, Selective laser melting of Ti–35Nb composite from elemental powder mixture: Microstructure, mechanical behavior and corrosion behavior, Mater. Sci. Eng. A. 760 (2019) 214–224. https://doi.org/10.1016/j.msea.2019.06.001.
[26] Q. Wang, C. Han, T. Choma, Q. Wei, C. Yan, B. Song, Y. Shi, Effect of Nb content on microstructure, property and in vitro apatite-forming capability of Ti-Nb alloys fabricated via selective laser melting, Mater. Des. 126 (2017) 268–277. https://doi.org/10.1016/j.matdes.2017.04.026.
[27] T. Nagase, T. Hori, M. Todai, S.-H. Sun, T. Nakano, Additive manufacturing of dense components in beta-titanium alloys with crystallographic texture from a mixture of pure metallic element powders, Mater. Des. 173 (2019) 107771. https://doi.org/10.1016/j.matdes.2019.107771.
[28] N. Soro, E.G. Brodie, A. Abdal-hay, A.Q. Alali, D. Kent, M.S. Dargusch, Additive manufacturing of biomimetic Titanium-Tantalum lattices for biomedical implant applications, Mater. Des. 218 (2022) 110688. https://doi.org/10.1016/j.matdes.2022.110688.
[29] E.G. Brodie, J. Richter, T. Wegener, T. Niendorf, A. Molotnikov, Low-cycle fatigue performance of remelted laser powder bed fusion (L-PBF) biomedical Ti25Ta, Mater. Sci. Eng. A. 798 (2020) 140228. https://doi.org/10.1016/j.msea.2020.140228.
[30] T. Zhang, Z. Huang, T. Yang, H. Kong, J. Luan, A. Wang, D. Wang, W. Kuo, Y. Wang, C.-T. Liu, In situ design of advanced titanium alloy with concentration modulations by additive manufacturing, Science. (2021). https://doi.org/10.1126/science.abj3770.
[31] R. Duan, S. Li, B. Cai, Z. Tao, W. Zhu, F. Ren, M.M. Attallah, In situ alloying based laser powder bed fusion processing of β Ti–Mo alloy to fabricate functionally graded composites, Compos. Part B Eng. 222 (2021) 109059. https://doi.org/10.1016/j.compositesb.2021.109059.
[32] S.A. Mantri, M.S.K.K.Y. Nartu, S. Dasari, A. Sharma, P. Agrawal, R. Salloom, F. Sun, E. Ivanov, K. Cho, B. McWilliams, S.G. Srinivasan, N.B. Dahotre, F. Prima, R. Banerjee, Suppression and reactivation of transformation and twinning induced plasticity in laser powder bed fusion additively manufactured Ti-10V-2Fe-3Al, Addit. Manuf. 48 (2021) 102406. https://doi.org/10.1016/j.addma.2021.102406.
[33] X. Chen, C. Qiu, Development of a novel metastable beta titanium alloy with ultrahigh yield strength and good ductility based on laser power bed fusion, Addit. Manuf. (2021) 102501. https://doi.org/10.1016/j.addma.2021.102501.

[34] C. Qiu, Q. Liu, R. Ding, Significant enhancement in yield strength for a metastable beta titanium alloy by selective laser melting, Mater. Sci. Eng. A. 816 (2021) 141291. https://doi.org/10.1016/j.msea.2021.141291.
[35] L. Lilensten, Y. Danard, R. Poulain, R. Guillou, J.M. Joubert, L. Perrière, P. Vermaut, D. Thiaudière, F. Prima, From single phase to dual-phase TRIP-TWIP titanium alloys: Design approach and properties, Materialia. 12 (2020) 100700. https://doi.org/10.1016/j.mtla.2020.100700.
[36] T. de Terris, O. Andreau, P. Peyre, F. Adamski, I. Koutiri, C. Gorny, C. Dupuy, Optimization and comparison of porosity rate measurement methods of Selective Laser Melted metallic parts, Addit. Manuf. 28 (2019) 802–813. https://doi.org/10.1016/j.addma.2019.05.035.
[37] C. Qiu, N.J.E. Adkins, M.M. Attallah, Microstructure and tensile properties of selectively laser-melted and of HIPed laser-melted Ti–6Al–4V, Mater. Sci. Eng. A. 578 (2013) 230–239. https://doi.org/10.1016/j.msea.2013.04.099.
[38] W. Xu, M. Brandt, S. Sun, J. Elambasseril, Q. Liu, K. Latham, K. Xia, M. Qian, Additive manufacturing of strong and ductile Ti–6Al–4V by selective laser melting via in situ martensite decomposition, Acta Mater. 85 (2015) 74–84. https://doi.org/10.1016/j.actamat.2014.11.028.
[39] A. Mertens, S. Reginster, H. Paydas, Q. Contrepois, T. Dormal, O. Lemaire, J. Lecomte-Beckers, Mechanical properties of alloy Ti–6Al–4V and of stainless steel 316L processed by selective laser melting: influence of out-of-equilibrium microstructures, Powder Metall. 57 (2014) 184–189. https://doi.org/10.1179/1743290114Y.0000000092.
[40] G. Kasperovich, J. Hausmann, Improvement of fatigue resistance and ductility of TiAl6V4 processed by selective laser melting, J. Mater. Process. Technol. 220 (2015) 202–214. https://doi.org/10.1016/j.jmatprotec.2015.01.025.
[41] T. Vilaro, C. Colin, J.D. Bartout, As-Fabricated and Heat-Treated Microstructures of the Ti-6Al-4V Alloy Processed by Selective Laser Melting, Metall. Mater. Trans. A. 42 (2011) 3190–3199. https://doi.org/10.1007/s11661-011-0731-y.
[42] S. Leuders, M. Thöne, A. Riemer, T. Niendorf, T. Tröster, H.A. Richard, H.J. Maier, On the mechanical behaviour of titanium alloy TiAl6V4 manufactured by selective laser melting: Fatigue resistance and crack growth performance, Int. J. Fatigue. 48 (2013) 300–307. https://doi.org/10.1016/j.ijfatigue.2012.11.011.
[43] L. Facchini, E. Magalini, P. Robotti, A. Molinari, S. Höges, K. Wissenbach, Ductility of a Ti-6Al-4V alloy produced by selective laser melting of prealloyed powders, Rapid Prototyp. J. 16 (2010) 450–459. https://doi.org/10.1108/13552541011083371.
[44] H. Ali, L. Ma, H. Ghadbeigi, K. Mumtaz, In-situ residual stress reduction, martensitic decomposition and mechanical properties enhancement through high temperature powder bed pre-heating of Selective Laser Melted Ti6Al4V, Mater. Sci. Eng. A. 695 (2017) 211–220. https://doi.org/10.1016/j.msea.2017.04.033.
[45] J. Liu, Q. Sun, C. Zhou, X. Wang, H. Li, K. Guo, J. Sun, Achieving Ti6Al4V alloys with both high strength and ductility via selective laser melting, Mater. Sci. Eng. A. 766 (2019) 138319. https://doi.org/10.1016/j.msea.2019.138319.
[46] S. Pal, N. Gubeljak, R. Hudak, G. Lojen, V. Rajtukova, J. Predan, V. Kokol, I. Drstvensek, Tensile properties of selective laser melting products affected by building orientation and energy density, Mater. Sci. Eng. A. 743 (2019) 637–647. https://doi.org/10.1016/j.msea.2018.11.130.
[47] A. Dareh Baghi, S. Nafisi, R. Hashemi, H. Ebendorff-Heidepriem, R. Ghomashchi, Effective post processing of SLM fabricated Ti-6Al-4 V alloy: Machining vs thermal treatment, J. Manuf. Process. 68 (2021) 1031–1046. https://doi.org/10.1016/j.jmapro.2021.06.035.
[48] B. Gillham, A. Yankin, F. McNamara, C. Tomonto, D. Taylor, R. Lupoi, Application of the Theory of Critical Distances to predict the effect of induced and process inherent defects for SLM Ti-6Al-4V in high cycle fatigue, CIRP Ann. 70 (2021) 171–174. https://doi.org/10.1016/j.cirp.2021.03.004.
[49] C. Pauzon, T. Mishurova, S. Evsevleev, S. Dubiez-Le Goff, S. Murugesan, G. Bruno, E. Hryha, Residual stresses and porosity in Ti-6Al-4V produced by laser powder bed fusion as a function of process atmosphere and component design, Addit. Manuf. 47 (2021) 102340. https://doi.org/10.1016/j.addma.2021.102340.

[50] N. Kang, X. Lin, C. Coddet, X. Wen, W. Huang, Selective laser melting of low modulus Ti-Mo alloy: α/β heterogeneous conchoidal structure, Mater. Lett. 267 (2020) 127544. https://doi.org/10.1016/j.matlet.2020.127544.
[51] N. Kang, Y. Li, X. Lin, E. Feng, W. Huang, Microstructure and tensile properties of Ti-Mo alloys manufactured via using laser powder bed fusion, J. Alloys Compd. 771 (2019) 877–884. https://doi.org/10.1016/j.jallcom.2018.09.008.
[52] X.H. Min, S. Emura, K. Tsuchiya, T. Nishimura, K. Tsuzaki, Transition of multi-deformation modes in Ti–10Mo alloy with oxygen addition, Mater. Sci. Eng. A. 590 (2014) 88–96. https://doi.org/10.1016/j.msea.2013.10.010.
[53] P.J. Bania, Beta titanium alloys and their role in the titanium industry, JOM. 46 (1994) 16–19. https://doi.org/10.1007/BF03220742.
[54] F. Huber, T. Papke, C. Kauffmann, R. Rothfelder, P. Krakhmalev, M. Merklein, M. Schmidt, Systematic exploration of the L-PBF processing behavior and resulting properties of β-stabilized Ti-alloys prepared by in-situ alloy formation, Mater. Sci. Eng. A. 818 (2021) 141374. https://doi.org/10.1016/j.msea.2021.141374.
[55] I. Yadroitsev, P. Krakhmalev, I. Yadroitsava, Titanium Alloys Manufactured by In Situ Alloying During Laser Powder Bed Fusion, JOM. 69 (2017) 2725–2730. https://doi.org/10.1007/s11837-017-2600-7.
[56] Y. Chen, L. Xu, Z. Liu, F. Kong, Z. Chen, Microstructures and properties of titanium alloys Ti-Mo for dental use, Trans. Nonferrous Met. Soc. China. 16 (2006) s824–s828. https://doi.org/10.1016/S1003-6326(06)60308-7.
[57] R.P. Kolli, A. Devaraj, A Review of Metastable Beta Titanium Alloys, Metals. 8 (2018) 506. https://doi.org/10.3390/met8070506.
[58] R. Davis, H.M. Flower, D.R.F. West, Martensitic transformations in Ti-Mo alloys, J. Mater. Sci. 14 (1979) 712–722. https://doi.org/10.1007/BF00772735.
[59] L. Thijs, F. Verhaeghe, T. Craeghs, J.V. Humbeeck, J.-P. Kruth, A study of the microstructural evolution during selective laser melting of Ti–6Al–4V, Acta Mater. 58 (2010) 3303–3312. https://doi.org/10.1016/j.actamat.2010.02.004.
[60] B.E. Carroll, T.A. Palmer, A.M. Beese, Anisotropic tensile behavior of Ti–6Al–4V components fabricated with directed energy deposition additive manufacturing, Acta Mater. 87 (2015) 309–320. https://doi.org/10.1016/j.actamat.2014.12.054.
[61] A. Yadollahi, N. Shamsaei, Additive manufacturing of fatigue resistant materials: Challenges and opportunities, Int. J. Fatigue. 98 (2017) 14–31. https://doi.org/10.1016/j.ijfatigue.2017.01.001.
[62] I. Yadroitsev, A. Gusarov, I. Yadroitsava, I. Smurov, Single track formation in selective laser melting of metal powders, J. Mater. Process. Technol. 210 (2010) 1624–1631. https://doi.org/10.1016/j.jmatprotec.2010.05.010.
[63] J. Gheysen, M. Marteleur, C. van der Rest, A. Simar, Efficient optimization methodology for laser powder bed fusion parameters to manufacture dense and mechanically sound parts validated on AlSi12 alloy, Mater. Des. 199 (2021) 109433. https://doi.org/10.1016/j.matdes.2020.109433.
[64] R. Duan, S. Li, B. Cai, W. Zhu, F. Ren, M.M. Attallah, A high strength and low modulus metastable β Ti-12Mo-6Zr-2Fe alloy fabricated by laser powder bed fusion in-situ alloying, Addit. Manuf. 37 (2021) 101708. https://doi.org/10.1016/j.addma.2020.101708.
[65] C. de Formanoir, A. Brulard, S. Vivès, G. Martin, F. Prima, S. Michotte, E. Rivière, A. Dolimont, S. Godet, A strategy to improve the work-hardening behavior of Ti–6Al–4V parts produced by additive manufacturing, Mater. Res. Lett. 5 (2017) 201–208. https://doi.org/10.1080/21663831.2016.1245681.
[66] C. Su, H. Yu, Z. Wang, J. Yang, X. Zeng, Controlling the tensile and fatigue properties of selective laser melted Ti–6Al–4V alloy by post treatment, J. Alloys Compd. 857 (2021) 157552. https://doi.org/10.1016/j.jallcom.2020.157552.
[67] J. Han, J. Yang, H. Yu, J. Yin, M. Gao, Z. Wang, X. Zeng, Microstructure and mechanical property of selective laser melted Ti6Al4V dependence on laser energy density, Rapid Prototyp. J. 23 (2017) 217–226. https://doi.org/10.1108/RPJ-12-2015-0193.

[68] A. Dareh Baghi, S. Nafisi, R. Hashemi, H. Ebendorff-Heidepriem, R. Ghomashchi, Experimental realisation of build orientation effects on the mechanical properties of truly as-built Ti-6Al-4V SLM parts, J. Manuf. Process. 64 (2021) 140–152. https://doi.org/10.1016/j.jmapro.2021.01.027.
[69] B. Vrancken, L. Thijs, J.-P. Kruth, J. Van Humbeeck, Heat treatment of Ti6Al4V produced by Selective Laser Melting: Microstructure and mechanical properties, J. Alloys Compd. 541 (2012) 177–185. https://doi.org/10.1016/j.jallcom.2012.07.022.
[70] M. Simonelli, Y.Y. Tse, C. Tuck, On the Texture Formation of Selective Laser Melted Ti-6Al-4V, Metall. Mater. Trans. A. 45 (2014) 2863–2872. https://doi.org/10.1007/s11661-014-2218-0.
[71] F. Sun, J.Y. Zhang, P. Vermaut, D. Choudhuri, T. Alam, S.A. Mantri, P. Svec, T. Gloriant, P.J. Jacques, R. Banerjee, F. Prima, Strengthening strategy for a ductile metastable β-titanium alloy using low-temperature aging, Mater. Res. Lett. 5 (2017) 547–553. https://doi.org/10.1080/21663831.2017.1350211.
[72] M.J. Lai, T. Li, D. Raabe, ω phase acts as a switch between dislocation channeling and joint twinning- and transformation-induced plasticity in a metastable β titanium alloy, Acta Mater. 151 (2018) 67–77. https://doi.org/10.1016/j.actamat.2018.03.053.
[73] J. Gao, A.J. Knowles, D. Guan, W.M. Rainforth, ω phase strengthened 1.2GPa metastable β titanium alloy with high ductility, Scr. Mater. 162 (2019) 77–81. https://doi.org/10.1016/j.scriptamat.2018.10.043.
[74] S. Leuders, T. Lieneke, S. Lammers, T. Tröster, T. Niendorf, On the fatigue properties of metals manufactured by selective laser melting — The role of ductility, J. Mater. Res. 29 (2014) 1911–1919. https://doi.org/10.1557/jmr.2014.157.
[75] M. Koike, P. Greer, K. Owen, G. Lilly, L.E. Murr, S.M. Gaytan, E. Martinez, T. Okabe, Evaluation of Titanium Alloys Fabricated Using Rapid Prototyping Technologies—Electron Beam Melting and Laser Beam Melting, Materials. 4 (2011) 1776–1792. https://doi.org/10.3390/ma4101776.
[76] D.A. Hollander, M. von Walter, T. Wirtz, R. Sellei, B. Schmidt-Rohlfing, O. Paar, H.-J. Erli, Structural, mechanical and in vitro characterization of individually structured Ti–6Al–4V produced by direct laser forming, Biomaterials. 27 (2006) 955–963. https://doi.org/10.1016/j.biomaterials.2005.07.041.
[77] B. Dutta, F.H. (Sam) Froes, The Additive Manufacturing (AM) of titanium alloys, Met. Powder Rep. 72 (2017) 96–106. https://doi.org/10.1016/j.mprp.2016.12.062.
[78] D. Zhang, D. Qiu, M.A. Gibson, Y. Zheng, H.L. Fraser, D.H. StJohn, M.A. Easton, Additive manufacturing of ultrafine-grained high-strength titanium alloys, Nature. 576 (2019) 91–95. https://doi.org/10.1038/s41586-019-1783-1.
[79] M. Masoomi, S.M. Thompson, N. Shamsaei, Laser powder bed fusion of Ti-6Al-4V parts: Thermal modeling and mechanical implications, Int. J. Mach. Tools Manuf. 118–119 (2017) 73–90. https://doi.org/10.1016/j.ijmachtools.2017.04.007.
[80] P. Wang, X. Tan, M.L.S. Nai, J. Wu, J. Wei, Deformation induced nanoscale twinning improves strength and ductility in additively manufactured titanium alloys, Mater. Sci. Eng. A. 833 (2022) 142568. https://doi.org/10.1016/j.msea.2021.142568.
[81] Z. Sun, X. Tan, S.B. Tor, C.K. Chua, Simultaneously enhanced strength and ductility for 3D-printed stainless steel 316L by selective laser melting, NPG Asia Mater. 10 (2018) 127–136. https://doi.org/10.1038/s41427-018-0018-5.
[82] P. Agrawal, S. Thapliyal, S.S. Nene, R.S. Mishra, B.A. McWilliams, K.C. Cho, Excellent strength-ductility synergy in metastable high entropy alloy by laser powder bed additive manufacturing, Addit. Manuf. 32 (2020) 101098. https://doi.org/10.1016/j.addma.2020.101098.